Efficient Feature-Based Nonrigid Registration of Multiphase Liver CT Volumes

Dongjin Kwon[1], Il Dong Yun[2], Kyoung Ho Lee[3], and Sang Uk Lee[1]
[1]School of EECS, Seoul Nat'l Univ., Seoul, 151-742, Korea
[2]School of EIE, Hankuk Univ. of F. S., Yongin, 449-791, Korea
[3]Dept. of Radiology, Seoul Nat'l Univ. Bundang Hosp., Seongnam, 463-707, Korea
djk@cvl.snu.ac.kr, yun@hufs.ac.kr, kholee@snubhrad.snu.ac.kr, sanguk@ipl.snu.ac.kr

Abstract

This paper presents an efficient feature-based nonrigid registration method for multiphase liver CT volumes. While radiologists routinely examine multiphase liver CT to detect hepatic diseases, they usually search corresponding points between 3D CT volumes by visual inspections using 2D slice images. As the liver is a deformable organ, there exist complex nonrigid transformations between liver CT volumes obtained at difference time points (phases). We introduce a fully automatic registration application for multiphase liver CT volumes. For two given liver CT volumes, we extract 3D features with their descriptors, and estimate correspondences by finding nearest neighbor in descriptor space. An energy function is constructed using the correspondence information and the smoothness measure of free-form deformation model based on B-splines. We integrate an approximated smoothness energy function and a robust correspondence energy estimator controlled by the confidence radius of the matching distance in this energy model. The energy function is optimized by sequentially reducing the confidence radius, and outlier correspondences are discarded systematically during convergence. We propose a highly efficient optimization procedure using the preconditioned nonlinear conjugate gradient method. In the experiments, we will provide quantitative and qualitative results on synthetic and clinical data sets.

1 Introduction

Multiphase liver CT is a standard-of-practice in hepatic imaging, which exploits the temporal difference in the contrast material delivery to the liver between arterial and portal phases. We show a multiphase liver CT example in Figure 1. By obtaining CT volumes at different phases after intravenous bolus injection of contrast material, this technique depicts the hemodynamic characteristics of different hepatic focal lesions, such as hepatocellular carcinoma (HCC) and metastases [5]. In this technique, radiologists' task is identifying a lesion that shows a dynamic enhancement pattern different from that of the background liver (lesion detection), and then classifying this enhancement pattern (lesion characterization). In general, this interpretation process involves a series of searching 2D slice images for the correspondences of different phases showing the same hepatic region,

BMVC 2008 doi:10.5244/C.22.36

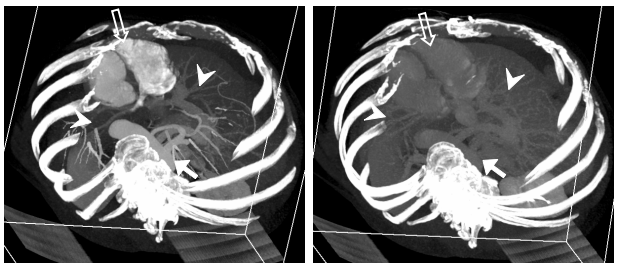

(a) Arterial Phase (b) Portal Phase

Figure 1: A Multiphase liver CT example. The liver CT volumes obtained at arterial and portal phases are shown in (a) and (b), respectively. The figures show the intensity differences between phases of the liver (arrowhead), the heart (open arrow), the aorta (arrow), and so on. The volumes are displayed using maximum intensity projection.

and then visually comparing them. If this process is automated by a registration method, it would significantly enhance the radiologists' performance.

However, the registration for multiphase liver CT images has following difficulties: The liver is a highly deformable organ and deformed passively by complex movements of the heart and the lung on top, the rib cage on side, and the other abdominal organs on bottom. Furthermore, intensity difference on the liver between phases is large and diseased hepatic texture is usually noisy. One can clearly see intensity differences of hepatic regions between phases in Figure 1.

In this paper, we will propose an efficient feature-based registration method for multiphase liver CT volumes to solve above problems. As pointed out by Masutani et al. [8], one of the most critical problems for nonrigid registration method is cost for computational time. So we lay weight on the efficiency of registration methods, and we decided to follow feature-based registration approaches. The summary of the proposed method is following: The features are detected using 3D Förstner corner detector [3], and descriptors are constructed using locally structured gradient histogram [7]. To find the sufficient number of features in the liver area, we apply adaptive thresholding for the cornerness weights considering the liver Hounsfield Unit (HU) statistics. The correspondences between two feature sets are obtained by finding the nearest neighbor in the descriptor space. Since there exist similar structures or textures in the abdominal region, the correspondences usually have a significant number of outliers. To discard outliers systematically, we integrate a robust estimator [9] to the energy function, and optimize the energy by sequentially reducing the confidence radius of the robust estimator. The deformation pattern of the whole abdominal region including the liver is represented by the free-form deformation (FFD) model based on B-splines [6], and an efficient approximated deformation energy is incorporated in the energy function. For energy optimization, we propose a highly efficient optimization method using the preconditioned nonlinear conjugate gradient method [13] utilizing exact derivative equations tailored to our energy function. The registration procedure is illustrated in Figure 2.

In the literature, there are many papers describing medical image registration methods [15]. Rueckert et al. [12] used normalized mutual information for the similarity measure and FFD model based on B-splines for modeling the deformation pattern. Rohlfing et

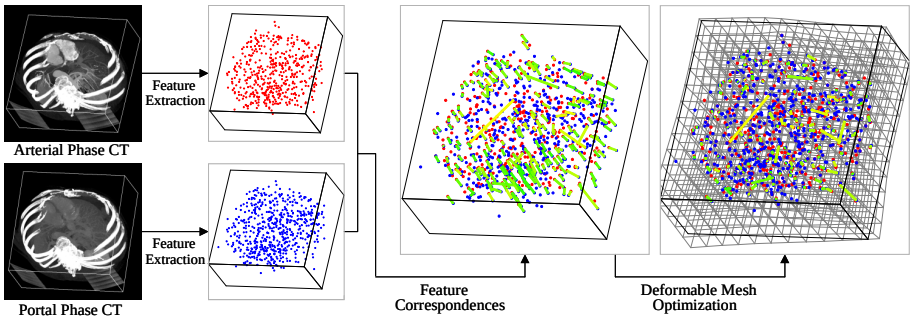

Figure 2: The registration procedure for multiphase liver CT volumes. In the feature extraction results, we show only feature locations while features consist of locations and descriptors. In the feature correspondence results, we show correspondences as green lines and marks brighter color for higher weight. In the mesh optimization results, we show optimized mesh for the portal phase CT. For visualization purpose, results are generated using quarter sized volumes. The results for original size volumes have more features and finer meshes.

al. [10] presented a technique for modeling liver motion during the respiratory cycle using a modified implementation of [12]. The execution time of [12] takes about several hours for the data sets we interested [8], however our target method requires only few minutes on the same data. As we are interested to fast methods to register multiphase CT volumes, we do not experiment using intensity-based methods in this paper. Chui and Rangarajan [1] developed a nonrigid point matching algorithm named TPS-RPM (thin-plate spline - robust point matching) which estimates correspondence and the spatial mapping jointly. As they only consider feature location to find correspondences, their method would not be an effective approach for our application. However we adopt an iterative optimization strategy similar to their deterministic annealing procedure. Urschler et al. [14] used local and global 3D descriptors for robust feature matching and calculated a dense displacement field using a thin-plate spline (TPS) model. As their method would be potentially suitable for our application and we will compare the proposed method to this one.

2 Registration Algorithm

2.1 Feature Extraction

Feature Location: The 3D interest point detector is a well established research topic in medical imaging, and comparative experimental results of various detecting methods are provided in [4]. We select 3D Förstner corner detector [3] for finding features as it shows good empirical performance. As we always know the exact physical dimension of CT volumes, we do not need to consider scale invariant detector in this case. The cornerness F of a given volume g at (x,y,z) is defined by following equation:

$$F(x,y,z) = det(\underline{C})/trace(\underline{C}^{adj}) \quad \text{with} \quad \underline{C} = \overline{\nabla g(\nabla g)^T} \tag{1}$$

where $\underline{C}^{adj}$ is adjugate matrix of $\underline{C}$, ∇g is the gradient of g obtained using the 3D Sobel

operator, and $\overline{\nabla g(\nabla g)^T}$ represents the average of $\nabla g(\nabla g)^T$ in a 3×3×3 voxel window centered at (x,y,z). We define the location of a feature as the point with the local maximum of F within a 5×5×5 window. Here, we point out that points with maxima F below the given cornerness threshold F_{th} are discarded. In the abdominal region, F of the bone and lung has usually higher values than the liver area, so a single F_{th} value limiting the total number of features can remove many useful features in the liver area. We resolved this problem by applying a different threshold $F_{th_{liver}}$ in the candidate liver area found by comparing the empirical liver HU statistics. For multiphase liver CT, the liver HU is ranging from 0 HU to 150 HU. Finally we can obtain a sufficient number of features that spread out evenly. In the experiments, $F_{th} = 1000$ and $F_{th_{liver}} = 50$ are empirically chosen.

Feature Descriptor: For given feature locations, we construct the descriptor using locally structured 3D gradient histogram which is a well established method in 2D images [7]. Firstly, we find the maximum gradient orientation using a 3D gradient vector histogram constructed in the 16×16×16 window centered at the feature location. Then we make gradient histogram having 4×4×4 grid rotated to the maximum of orientation, each bin has 4×4×4 window. The gradient orientation (θ,ϕ) in the spherical coordinate (ρ,θ,ϕ) is quantized to 4×8 histogram bins (considering $0 \le \theta \le \pi, 0 \le \phi \le 2\pi$, bin size is $\pi/4 \times \pi/4$) and Gaussian weighted ρ is added to each corresponding bin. Above window and bin sizes are chosen based on an analysis on 2D images [7]. Finally a 2048-dimensional descriptor (grid size × histogram bin number) is constructed after L_2-norm normalization.

Correspondences: The correspondences between two feature sets are established by finding nearest neighbor (NN) in the 2048-dimensional descriptor space. We compare all the candidate features in a given distance boundary and the corresponding feature with minimum distance d_{min} in the descriptor space is selected. Additionally we reject all matches when the distance ratio (first over second closest distance) is greater than d_r and d_{min} is larger than the maximum possible distance d_{th}. We used $d_r = 0.8$ based on an analysis on 2D images [7]. Although conventional feature-based approaches minimize the number of outlier correspondences by using a distance threshold, the threshold value and its determination depends on applications. We use all NN information in the energy construction. In the following, one of two given volumes is called as reference and the other as input. We define C as a set of correspondences $c = (c_i, c_r)$ between the reference c_r and input c_i features. The weight of each correspondence $w_c \in [0,1]$ is defined as $1 - d_{min}/d_{th}$, and a larger value means a higher reliable matching.

2.2 Deformable Mesh

For an input volume, we construct a control point grid Φ, which is a lattice of control points ϕ with uniform spacing δ. If S represents a state of all mesh vertices at some time, a transformed point $T_S(\mathbf{x})$ of point $\mathbf{x}$ is represented by the following conventional FFD model based on B-splines [6]:

$$T_S(\mathbf{x}) = \sum_{l=0}^{3}\sum_{m=0}^{3}\sum_{n=0}^{3} B_l(u)B_m(v)B_n(w)\phi^S_{i+l,j+m,k+n} \tag{2}$$

where ϕ^S are control points at state S, $i = \lfloor x/\delta \rfloor + 1$, $j = \lfloor y/\delta \rfloor + 1$, $k = \lfloor z/\delta \rfloor + 1$, $u = x/\delta - \lfloor x/\delta \rfloor$, $v = y/\delta - \lfloor y/\delta \rfloor$, $w = z/\delta - \lfloor z/\delta \rfloor$, and B_l is the lth basis function of

the uniform cubic B-spline [12].

2.3 Energy Function

For a given state S and correspondences C, we define the energy E as

$$E(S,C,r) = \lambda_D E_D(S) + E_C(S,C,r) \tag{3}$$

where E_D is the deformation energy, E_C is the correspondence energy, λ_D is the control parameter of the regularity of the mesh, and r is the confidence radius.

Deformation Energy: We define the deformation energy as the approximation of the sum of squared second derivatives of the x, y, z coordinates. If we define L as an index set of successive collinear three vertices, the deformation energy can be defined as

$$\begin{aligned} E_D(S) &= \sum_{(i,j,k)\in L} (-x_i + 2x_j - x_k)^2 + (-y_i + 2y_j - y_k)^2 + (-z_i + 2z_j - z_k)^2 \\ &= \mathbf{X^T K X} + \mathbf{Y^T K Y} + \mathbf{Z^T K Z} \approx \int_D \left(\left\| \frac{\partial^2 T_S}{\partial x^2} \right\|^2 + \left\| \frac{\partial^2 T_S}{\partial y^2} \right\|^2 + \left\| \frac{\partial^2 T_S}{\partial z^2} \right\|^2 \right) d\mathbf{x} \end{aligned} \tag{4}$$

where $\mathbf{X}$, $\mathbf{Y}$, $\mathbf{Z}$ are row ordered matrices of the x, y, z coordinates of the mesh control points at state S, respectively. $\mathbf{K}$ is constructed from $\tilde{\mathbf{K}}^\mathbf{T}\tilde{\mathbf{K}}$ where $\tilde{\mathbf{K}}$ is a matrix containing one row per triplet in L and one column per mesh vertex. In detail, the r^{th} row of $\tilde{\mathbf{K}}$ corresponding to triplet (i,j,k) is defined as follows:

$$\tilde{\mathbf{K}}_{ri} = -1,\ \tilde{\mathbf{K}}_{rj} = 2,\ \tilde{\mathbf{K}}_{rk} = -1, \tilde{\mathbf{K}}_{rc} = 0 \quad \text{for} \quad c \neq i,j,k\,. \tag{5}$$

Correspondence Energy: We define the correspondence energy as

$$E_C(S,C,r) = -\sum_{c\in C} w_c \rho\,(d,r) \quad \text{with} \quad \rho\,(d,r) = \begin{cases} \frac{3(r^2-d^2)}{4r^3} & d < r \\ 0 & otherwise \end{cases} \tag{6}$$

where $d = \|c_r - T_S(c_i)\|$, and ρ is the robust estimator [9]. The robust estimator has following characteristics: If r is large, the weights of most of the correspondences will be summed in the energy; if r is small, the weights of only selected correspondences will be used. Given C and r, minimizing E_C represents the mesh being deformed so that input feature locations coincide with the corresponding reference feature locations.

2.4 Optimization

Efficient Optimization Method: For minimizing E for fixed r, we propose to use the preconditioned nonlinear conjugate gradient method [13]. The complete pseudo code of the optimization procedure is shown in Algorithm 1. In this procedure, the Newton-Raphson method is used for the general line search (lines 5∼8), and the Polak-Ribière scheme (line 11) is used for quick convergence [13]. As the first and second partial derivatives of the energy (3) can be calculated analytically, the optimization can be implemented efficiently. The preconditioner matrix $\mathbf{M}$ uses second partial derivatives (lines 2,10). The

Algorithm 1 Optimize $E(S,C,r)$ Using Nonlinear Conjugate Gradient Method

$\mathbf{r} = (-\partial E/\partial \mathbf{X}, -\partial E/\partial \mathbf{Y}, -\partial E/\partial \mathbf{Z})$
$\mathbf{s} = \mathbf{M^{-1}r}$, $\mathbf{d} = \mathbf{s}$, $\delta^{\mathbf{new}} = \mathbf{r^T d}$, $\delta^{\mathbf{0}} = \delta^{\mathbf{new}}$ ▷ We let $\mathbf{M} = \partial^2 E/\partial \mathbf{X}^2$.
while $\delta_x^{new} > \varepsilon^2 \delta_x^0$ and $\delta_y^{new} > \varepsilon^2 \delta_y^0$ and $\delta_z^{new} > \varepsilon^2 \delta_z^0$ **do**
  $\delta^{\mathbf{d}} = \mathbf{d^T d}$
  repeat
    $\alpha = (-\frac{[\partial E/\partial \mathbf{X}]^T \mathbf{d_X}}{\mathbf{d_X^T}[\partial^2 E/\partial \mathbf{X}^2]\mathbf{d_X}}, -\frac{[\partial E/\partial \mathbf{Y}]^T \mathbf{d_Y}}{\mathbf{d_Y^T}[\partial^2 E/\partial \mathbf{Y}^2]\mathbf{d_Y}}, -\frac{[\partial E/\partial \mathbf{Z}]^T \mathbf{d_Z}}{\mathbf{d_Z^T}[\partial^2 E/\partial \mathbf{Z}^2]\mathbf{d_Z}})$
    $(\mathbf{X},\mathbf{Y},\mathbf{Z}) = (\mathbf{X},\mathbf{Y},\mathbf{Z}) + \alpha \cdot \mathbf{d}$
  until $\alpha_x^2 \delta_x^d > \varepsilon^2$ and $\alpha_y^2 \delta_y^d > \varepsilon^2$ and $\alpha_z^2 \delta_z^d > \varepsilon^2$
  $\mathbf{r} = (-\partial E/\partial \mathbf{X}, -\partial E/\partial \mathbf{Y}, -\partial E/\partial \mathbf{Z})$
  $\delta^{\mathbf{old}} = \delta^{\mathbf{new}}$, $\delta^{\mathbf{mid}} = \mathbf{r^T s}$, $\mathbf{s} = \mathbf{M^{-1}r}$, $\delta^{\mathbf{new}} = \mathbf{r^T s}$
  $\beta = (\frac{\delta_x^{new} - \delta_x^{mid}}{\delta_x^{old}}, \frac{\delta_y^{new} - \delta_y^{mid}}{\delta_y^{old}}, \frac{\delta_z^{new} - \delta_z^{mid}}{\delta_z^{old}})$
  $\mathbf{d} = \mathbf{s} + \beta \cdot \mathbf{d}$
end while

Algorithm 2 Optimize $E(S,C)$ Using Confidence Radius Scheduling

$r = r_0$
while $r \geq r_e$ **do**
  Optimize $E(S,C,r)$ ▷ Algorithm 1.
  $r = \eta \cdot r$ ▷ η is an attenuation constant in $(0,1)$.
end while

first derivative of the x coordinate are computed using the following equations:

$$\frac{\partial E}{\partial \mathbf{X}} = \lambda_D \mathbf{K}\mathbf{X} + \frac{\partial E_C}{\partial \mathbf{X}} , \tag{7}$$

$$\frac{\partial E_C}{\partial x_{\phi_{l,m,n}}} = \frac{3}{2r^3} \sum_{c \in C} w_c (x_{T_S(c_i)} - x_{c_r}) B_{l-i}(u) B_{m-j}(v) \cdot B_{n-k}(w) . \tag{8}$$

And the second derivative of the x coordinate are computed using the following equations:

$$\frac{\partial^2 E}{\partial \mathbf{X}^2} = \lambda_D \mathbf{K} + \frac{\partial^2 E_C}{\partial \mathbf{X}^2} , \tag{9}$$

$$\frac{\partial^2 E_C}{\partial x_{\phi_{p,q,r}} \partial x_{\phi_{l,m,n}}} = \frac{3}{2r^3} \sum_{c \in C} w_c B_{l-i}(u) B_{m-j}(v) \cdot B_{n-k}(w) B_{p-i}(u) B_{q-j}(v) B_{r-k}(w) . \tag{10}$$

In above equations, the summation is taken on the condition of $d < r$ and $0 \leq l-i, m-j, n-k, p-i, q-j, r-k \leq 3$. The derivatives for y and z coordinate can be similarly calculated.

Optimization Strategy: The whole optimization procedure for minimizing the energy (3) is shown in Algorithm 2. When r is large, E_D has a larger effect than E_C, so the mesh deforms rigidly. As r decreases, E_C becomes progressively more effective than E_D and the mesh bends to the correct matches. The effect of outliers diminishes as r decreases. In the experiments, $r_0 = 512$, $r_e = 0.5$, $\eta = 0.5$ is used.

Table 1: Results on synthetic data sets

Measure \ Data Set		SA_1	SP_1	SA_2	SP_2	SA_3	SP_3	SA_4	SP_4	SA_5	SP_5
$RMSD_{init}$	[HU]	291.4	275.8	240.5	245.7	247.1	264.9	179.2	179.2	330.5	381.3
$RMSD_{f_{TPS}}$	[HU]	55.1	54.7	62.3	54.4	59.3	72.1	60.2	66.3	60.4	48.8
$RMSD_{f_{prop}}$	[HU]	49.0	41.5	40.2	36.4	46.8	45.0	50.4	51.6	36.0	34.9
$RMS_{disp.f_{TPS}}$	[mm]	5.57	5.85	12.27	9.72	7.27	8.37	6.19	6.78	8.16	5.78
$RMS_{disp.f_{prop}}$	[mm]	1.08	1.18	1.80	1.54	2.44	2.34	1.59	1.43	1.11	1.15
$MAX_{disp.f_{TPS}}$	[mm]	61.53	61.33	65.54	65.64	49.92	52.48	52.97	52.20	48.82	54.78
$MAX_{disp.f_{prop}}$	[mm]	8.64	8.48	13.48	10.98	26.13	23.72	16.22	14.61	6.90	8.69
# correspondences		2883	3047	4663	4810	3960	3690	3116	3143	2472	2398

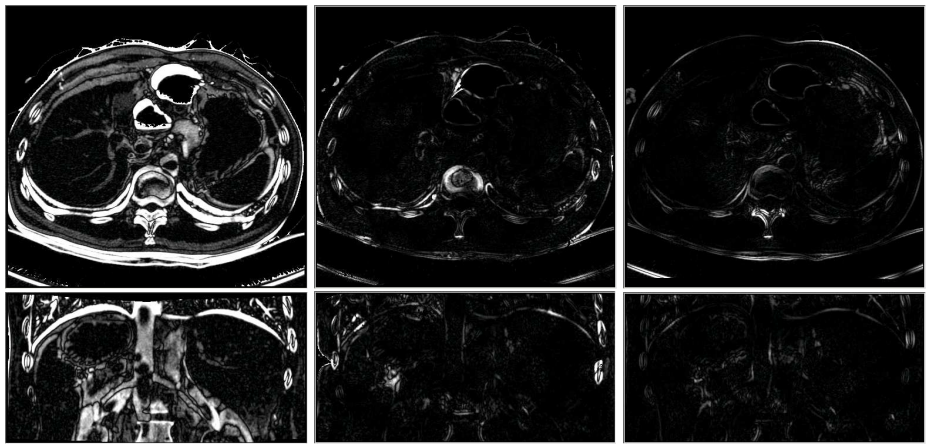

(a) (b) (c)

Figure 3: Intensity difference images ($|A_3 - A_3^{reg}|$) in synthetic data set SA_3: (a) before registration, (b) after registration using f_{TPS}, and (c) after registration using f_{prop}. The upper row is axial sections and the lower is coronal sections.

3 Experiments

To verify robustness, the proposed method, denoted f_{prop}, is compared with another feature based method, denoted f_{TPS}, which uses the same feature extraction and correspondences result with f_{prop} while the dense deformation field is estimated using the approximated thin-plate spline (TPS) method [11]. The test CT volumes are scanned at the arterial (A_i) and the portal (P_i) phase in the same patient having index i during dynamic contrast enhancement, and a total of five A and P sets are used. The volume size of test CT volumes are $512\times512\times S_z$ where S_z ranges 176 to 343. For mesh sizes, $\delta = 32$ (voxel unit, 17$\sim$22 mm depends on data sets) is used, and radiologists confirm that it is sufficiently fine to our application. For regularization parameters, f_{prop} uses $\lambda_D = 0.002$ and f_{TPS} uses 0.005 which are performed best. All experiments are performed on an Intel Pentium 4, 3.6 GHz machine with 3.12 GB RAM.

3.1 Synthetically Deformed Data

Since it is very difficult to model the complex organ movements in the abdomen, we created synthetically deformed data using the following method: For two given CT vol-

Table 2: Results on clinical data sets

Measure \ Data Set		C_1	C_2	C_3	C_4	C_5
$RMS_{disp_{land},f_{TPS}}$	[mm]	8.35	7.90	8.85	6.67	6.43
$RMS_{disp_{land},f_{prop}}$	[mm]	3.28	3.62	5.09	3.94	3.74
$MAX_{disp_{land},f_{TPS}}$	[mm]	46.85	39.88	29.09	25.99	34.13
$MAX_{disp_{land},f_{prop}}$	[mm]	11.23	12.95	24.36	18.00	15.19
# manual landmarks		230	300	283	205	254
# correspondences		1408	2184	1648	1355	956

(a) (b) (c)

Figure 4: Registration results of (a) arterial A_2 and (b) portal phase P_2 volumes in clinical data set C_2 using f_{prop}. (c) The signed difference image $A_2 - P_2^{reg}$ depicts a hypervascular hepatocellular carcinoma (arrow) with better visual contrast.

umes A_i and P_i, a radiologist manually marks $205 \sim 300$ evenly distributed corresponding landmarks by visual inspection. Using these correspondences, the dense synthetic deformation field $A_i \rightarrow P_i$ and $P_i \rightarrow A_i$ is calculated from the TPS interpolation assuming isotropic landmark errors [11]. We generate synthetically deformed volumes A_i^{syn} from A_i using $A_i \rightarrow P_i$ and P_i^{syn} from P_i using $P_i \rightarrow A_i$, and make two test sets $SA_i = \{A_i, A_i^{syn}\}$ and $SP_i = \{P_i, P_i^{syn}\}$. From test set SA_i (SP_i), we generate registered volume A_i^{reg} (P_i^{reg}) from A_i^{syn} (P_i^{syn}) after constructing the deformation field $A_i^{syn} \rightarrow A_i^{reg}$ ($P_i^{syn} \rightarrow P_i^{reg}$) using each algorithm.

The experimental results are shown in Table 1 where the measuring quantity is adopted from [14]. In Table 1, $RMSD_{init}$, $RMSD_{f_{TPS}}$, and $RMSD_{f_{prop}}$ are the root mean square (RMS) of the intensity difference before registration, after registration using f_{TPS}, and after using f_{prop}, respectively. RMS_{disp} and MAX_{disp} for each method are RMS and maximum of the lengths of displacement difference vectors between ground truth vectors $P \rightarrow A$ ($A \rightarrow P$) and generated vectors $A^{syn} \rightarrow A^{reg}$ ($P^{syn} \rightarrow P^{reg}$) using each algorithm. In Figure 3, we show intensity difference images to comparing qualitative results.

3.2 Clinical Data

In clinical tests, we applied the proposed method to register the liver area scanned at the arterial (A_i) and the portal (P_i) phase volumes. From test set $C_i = \{A_i, P_i\}$, we generate registered volume P_i^{reg} from P_i after constructing the deformation field $P_i \rightarrow P_i^{reg}$ using each algorithm. Compared to the synthetic data tests, the intensity difference measure is meaningless in this case, because the intensity significantly changes for a corresponding

region between different contrast enhancement phases. Therefore, we measured only the statistics of landmark positions which were manually marked by a radiologist for correspondence information.

The results are shown in the Table 2, where $RMS_{disp_{land}}$ and $MAX_{disp_{land}}$ for each method are RMS and maximum of the lengths of the displacement difference vectors between manual landmark correspondence vectors $P \rightarrow A$ and generated vectors $P \rightarrow P^{reg}$ calculated on manual landmark positions in P only. In Figure 4, we show qualitative visual inspection.

4 Discussion

The mean values of $RMS_{disp,f_{TPS}}$ and $RMS_{disp,f_{prop}}$ are 7.60mm and 1.57mm in synthetic tests, and 7.64mm and 3.93mm in clinical tests. The proposed method f_{prop} performed better than the TPS-based registration approach f_{TPS} in every performance measure. Since the TPS model is basically a surface interpolation scheme using the basis function having infinite response, wrong correspondences always distort deformation patterns erroneously and have global influences. So outlier correspondences should be minimized before the TPS warping. However eliminating outliers by thresholding correspondence weights w_c is a heuristic procedure that depends on the correctness of the weight measure, and a high threshold value will also eliminate informative correspondences. $MAX_{disp,f_{TPS}}$ values in synthetic and clinical tests show the TPS-based registration approach can not handle outliers appropriately, so erroneous deformation patterns are obtained. The proposed method is systematically robust for correspondences including outliers using the energy minimization approach on the FFD model incorporating the robust estimator.

The proposed method can be implemented very efficiently since all matrices including $\mathbf{M}$ and $\mathbf{K}$ are sparse. Every matrix calculation is executed in the sparse form such as compressed column representation and $\mathbf{M}^{-1}$ in Algorithm 1 is implemented using a direct sparse matrix solver [2]. In clinical tests, the total execution time of the proposed method f_{prop} ranges 218s to 448s where approximately 30% of time is consumed in feature extraction, and 50% for matching and optimization, and 20% for transformed volume generation. The execution time of the TPS-based method f_{TPS} ranges 701s to 2265s. For mesh optimization, the time complexity of the proposed method is mainly depends on the size of mesh vertices, however the time complexity of TPS-based method is largely depends on the number of correspondences. For transformed volume generation, TPS-based method is slower than the proposed method as it has to calculate weights from basis functions using all correspondences.

5 Conclusions

In this paper, we introduced an automatic registration application for the multiphase liver CT and presented an efficient feature-based nonrigid registration method for this application. By experimental results using synthetic and clinical data sets, we discuss robustness and efficiency of the proposed method. Although we provided the experimental data on the multiphase liver CT registration, the proposed method is general and can be easily extended to another target organs. As the proposed method runs very fast compared to intensity-based methods, the deformation pattern from the proposed method might be

used to an initial transformation for the more time-consuming intensity-based methods to achieve better qualitative results.

Acknowledgements

This work was supported by the Korea Research Foundation Grant funded by the Korean Government(MOEHRD) (KRF-2006-311-D00168).

References

[1] H. Chui and A. Rangarajan. A new point matching algorithm for non-rigid registration. *Computer Vision and Image Understanding*, 89(2-3):114–141, 2003.

[2] Timothy A. Davis. Algorithm 832: UMFPACK V4.3 - an unsymmetric-pattern multifrontal method. *ACM Trans. Math. Softw.*, 30(2):196–199, 2004.

[3] W. Förstner. A feature based correspondence algorithm for image matching. *Int. Arch. Photogramm. Remote Sensing*, 26:150–166, 1986.

[4] Thomas Hartkens, Karl Rohr, and H. Siegfried Stiehl. Evaluation of 3D Operators for the Detection of Anatomical Point Landmarks in MR and CT Images. *Computer Vision and Image Understanding*, 86:118–136, 2002.

[5] K. H. Lee, B. I. Choi, J. K. Han, H. J. Jang, T. K. Kim, and M. C. Han. Nodular hepatocellular carcinoma: variation of tumor conspicuity on single-level dynamic scan and optimization of fixed delay times for two-phase helical CT. *J. Comput. Assist. Tomogr.*, 24(2):212–218, 2000.

[6] S. Lee, G. Wolberg, and S. Y. Shin. Scattered data interpolation with multilevel B-splines. *IEEE Trans. on Visualization and Computer Graphics*, 3(3):228–244, 1997.

[7] David G. Lowe. Distinctive Image Features from Scale-Invariant Keypoints. *Int. J. Computer Vision*, 60(2):91–110, 2004.

[8] Y. Masutani, K. Uozumi, M. Akahane, and K. Ohtomo. Liver CT image processing: A short introduction of the technical elements. *European Journal of Radiology*, 58(2):246–251, 2006.

[9] J. Pilet, V. Lepetit, and P. Fua. Fast Non-Rigid Surface Detection, Registration and Realistic Augmentation. *Int. J. Computer Vision*, 76(2):109–122, 2008.

[10] Torsten Rohlfing, Calvin R. Maurer, Walter G. O'Dell, and Jianhui Zhong. Modeling liver motion and deformation during the respiratory cycle using intensity-based nonrigid registration of gated MR images. *Medical Physics*, 31(3):427–432, 2004.

[11] Karl Rohr. Image Registration Based on Thin-Plate Splines and Local Estimates of Anisotropic Landmark Localization Uncertainties. In *MICCAI*, 1998.

[12] D. Rueckert, L. I. Sonoda, C. Hayes, D. L. G. Hill, M. O. Leach, and D. J. Hawkes. Nonrigid Registration Using Free-Form Deformations: Application to Breast MR Images. *IEEE Trans. Medical Imaging*, 18(8):712–721, 1999.

[13] J. R. Shewchuk. An Introduction to the Conjugate Gradient Method Without the Agonizing Pain. 1994.

[14] Martin Urschler, Joachim Bauer, Hendrik Ditt, and Horst Bischof. SIFT and Shape Context for Feature-Based Nonlinear Registration of Thoracic CT Images. In *Computer Vision Approaches to Medical Image Analysis*, pages 73–84, 2006.

[15] Barbara Zitova and Jan Flusser. Image registration methods: a survey. *Image and Vision Computing*, 21(11):977–1000, 2003.